Optics Letters

Discrimination of bimetallic alloy targets using femtosecond filament-induced breakdown spectroscopy in standoff mode

Abdul Kalam Shaik,[1] Ajmathulla,[2] and Venugopal Rao Soma[1,3,*]

[1]Advanced Centre of Research in High Energy Materials (ACRHEM), University of Hyderabad, Hyderabad 500046, Telangana, India
[2]School of Physics, University of Hyderabad, Hyderabad 500046, Telangana, India
[3]e-mail: soma_venu@uohyd.ac.in
*Corresponding author: soma_venu@yahoo.com

Received 24 May 2018; revised 20 June 2018; accepted 20 June 2018; posted 22 June 2018 (Doc. ID 332479); published 16 July 2018

The femtosecond filament-induced breakdown spectroscopy (FIBS) technique coupled with principal component analysis (PCA) is demonstrated for standoff (ST) analysis of metals, alloys (Al, Cu, brass, stainless steel), and bimetallic strips (Ag@Cu, Ag@Au with varying weight percentages). The experiments were performed by analyzing the filament-produced plasma at ~6.5 m from the laser. The plasma emissions were collected using a Schmidt–Cassegrain telescope (6″ f/10) at ~8 m away. The variations in intensities of persistent atomic transitions in the FIBS spectra clearly reflected the varying weight percentage in bimetallic strips. Furthermore, PCA was successfully utilized to discriminate the metals, alloys, and bimetallic strips batch wise and altogether. Our results demonstrate the capability of femtosecond ST-FIBS for ST analytical applications.

OCIS codes: (300.6365) Spectroscopy, laser induced breakdown; (320.7090) Ultrafast lasers; (320.2250) Femtosecond phenomena; (170.1580) Chemometrics.

https://doi.org/10.1364/OL.43.003465

Over the last couple of decades, the laser-induced breakdown spectroscopy (LIBS) technique has emerged as a potential spectroscopic technique for analysis of various samples in their unconventional state [1]. Rapid *in situ* multi-elemental analysis is the motive for LIBS applications in the field of investigation of minerals, rocks, and geochemical samples. Recent studies have demonstrated the LIBS applications in numerous fields such as material processing, food processing, pharmaceutical industry, plastic recycling industry, soil analysis, and checking the trace-level contamination in water [2]. Moreover, LIBS has also been used in the remote analysis of archeological sites, space applications, and detection of explosives, etc. [3,4]. Along with LIBS, laser-induced fluorescence has the potential for standoff (ST) trace analysis [5], albeit the setup becomes more critical with the involvement of dye lasers which are bulky and not easy to maintain. Traditionally, nanosecond pulses have been expansively utilized for remote analysis of aerosols, metallurgical industry, and planetary missions.

To date, remote analyses using nanosecond pulses have been demonstrated up to ~100 m [6,7]. However, femtosecond pulses seem to be advantageous for ST applications, as they can propagate several hundreds of meters to few kilometers by forming intense filaments delivering high intensities at remote locations. When femtosecond pulses propagate in air, a stable plasma channel called a "filament" will be formed due to the dynamical balance between Kerr self-focusing effect and plasma defocusing effect [8–10]. During the femtosecond filamentation in air, the laser intensities can reach up to 10^{13}–10^{14} W/cm^2, which are intense enough to ablate and create plasma, thus resulting in characteristic atomic and molecular emissions. Femtosecond filaments have a range of applications, from atmosphere sensing, analyzing metals, and chemical and biological agents, to label isotopes of nuclear materials (assisted with laser ablation molecular isotopic spectrometry) and detection of explosives in remote/ST configurations [8,11–13]. They can be potentially utilized for remote analysis in harsh environments, including polluted sites. In contrast, nanosecond pulses suffer from diffraction, or beam wandering and, thus, fail to deliver high intensities to remote locations [14]. Fujii *et al.* [11] utilized femtosecond LIBS, in combination with LIDAR (using terawatt pulses), to demonstrate the capability of remote sensing micro-particles in ambient air. Stelmaszczyk *et al.* [8] again utilized femtosecond terawatt pulses and demonstrated 90 m ST LIBS measurements of copper and iron targets. Interestingly, femtosecond pulses can be tailored (chirped) to improve the generated filaments which, in turn, improve the ablation efficiency [15]. Femtosecond pulse ablation characteristics such as no pulse-plasma interaction, minimal plasma-ambience interaction [16], diminished matrix effects, lesser heat affected zones, and smaller crater depths, are worthwhile for employing femtosecond filaments in ST applications [17]. *In situ* elemental analysis of minerals and alloys, and their classification at ST distances is interesting and challenging. In our earlier work, we successfully demonstrated the ST (up to 2 m) and remote (detector only at 8.5 m) detection capability of bulk explosives [18]. In this Letter, we establish ~6.5 m/ ~ 8 m (focusing/collection distance) ST discrimination of metals and

bimetallic alloys using femtosecond filament–induced breakdown spectroscopy in the ST mode (ST-FIBS). Furthermore, principal component analysis (PCA) was utilized to discriminate the bimetallic strips among themselves and from metals, and we obtained excellent classification in most of these cases.

A Ti:sapphire amplifier laser system (M/s Coherent, Libra, ~4 mJ, 1 kHz) delivering ~50 fs laser pulses and operating at 800 nm was employed to perform femtosecond ST-filament-induced breakdown spectroscopy (fs ST-FIBS) experiments. The femtosecond pulses with typically 2 mJ of energy were focused, using a two-lens configuration (L1 and L2), where the focusing distance could be varied by changing the distance between the two lenses. L1 is a plano-concave lens (PCV) of −50 cm focal length, and L2 is a plano-convex lens (PCX) of focal length 100 cm. Figure 1 depicts the schematic of fs ST-FIBS setup where femtosecond pulses were focused to form a filament of ~30 cm length at 6.5 m away (as measured from L2). The most intense part of the filament [19] was made to interact with the target's surface normally [20]. The details of the targets used in this Letter are summarized in Table 1.

The resulting plasma emissions were collected at a distance of ~8 m from the plasma using a Schmidt–Cassegrain telescope (6″ f/10, with effective light transmission in a visible region of 420–700 nm [21]) and coupled to an ANDOR Mechelle spectrometer (resolution of 0.05 at 500 nm, spectral window of 220–880 nm) attached with an ICCD through an optical fiber (600 μm diameter). Both the focusing, as well as the collection distances, are slightly different due to constraints in our lab and other experimental setups. Fs ST-FIBS spectra of all targets were recorded with a gate delay of 50 ns, gate width of 1 μs, ICCD gain of 2500, and exposure time of 1.5 s in an accumulation mode (6 accumulations) without any flat field correction. Thus, each spectrum is the result of plasma emissions from 9000 pulses (1500 × 6 = 9000 pulses). In this configuration, metals (Al, Cu), alloys (brass, stainless steel), and bimetallic strips (Ag@Cu, Ag@Au) were investigated. Pure bimetallic strips were locally made by blending Ag, Au and Ag, Cu in different weight percentages, and their homogeneity was confirmed by energy-dispersive x-ray spectroscopy data [22]. Figures 2(a) and 2(b) represent the stack plots of the fs ST-FIBS spectra of metals and alloys recorded with an ICCD gain of 1000 and 2500, respectively. Few Zinc atomic peaks were identified in copper and can be considered as impurity. The weak FIBS signal with a poor SNR, illustrated in Fig. 2(a), can be attributed to the plasma generating conditions by femtosecond filaments such as less crater depth, reduced ablation efficiency due to the energy distribution in energy reservoir, resulting in a cold plasma when compared with tight focused pulses [23,24]. However, for real-time ST applications, the filaments propagate much longer distances (few tens of meters to hundreds of meters) [25] in air and can interrogate the samples of interest at remote locations. Moreover, optimized usage of ICCD gain can result in significant improvement of the SNR by increasing the signal strength, as shown in Fig. 2(b). PCA was utilized to cluster and discriminate fs ST-FIBS spectra. PCA is a typical multivariate data analysis approach used to discriminate or classify by correlating the variables and extracting the similar features [26]. PCA finds its applications in various fields such as face recognition, image compression, pharmaceuticals, identification of tissue, and detection of explosives [27–30]. In PCA, the dimensionality of the multivariate dataset is reduced by calculating the eigenvectors of the covariance matrix of data and then projecting each variable on to the largest eigenvectors. Thus, principal components (PCs) are the new dimensions, which explain the variance present in the dataset and, thus, reduce the dimensionality. A PCA code was written in MATLAB to analyze the fs ST-FIBS spectra of metals and bimetallic targets batch wise. All the spectra were processed and normalized to the highest peak intensity

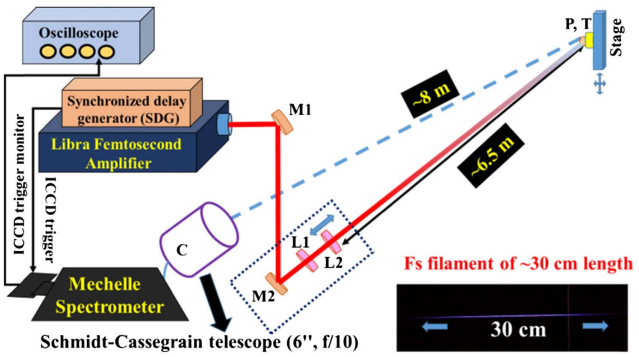

Fig. 1. Schematic of the laboratory-based ST FIBS setup (fs ST-FIBS) for investigation of metals and bimetallic targets. M, mirror; P, plasma; T, target; C, Schmidt–Cassegrain telescope; L1, PCV lens; L2, PCX lens. The inset depicts the femtosecond filament of ~30 cm in length captured by a DSLR camera with an exposure time of 30 s.

Table 1. Summary of the Samples Studied Using fs-FIBS Technique

Targets	Combinations	Weight %	Spectra #
Metals and Alloys	Aluminum (Al), Copper (Cu), Brass, Stainless Steel (SS)		25–30
Bimetallic strips	Ag @ Au ($Au_{20}Ag_{80}$ up to $Au_{80}Ag_{20}$, 7 combinations)	$Au_{20}Ag_{80}$	13–15
		$Au_{30}Ag_{70}$	
		$Au_{40}Ag_{60}$	
		$Au_{50}Ag_{50}$	
		$Au_{60}Ag_{40}$	
		$Au_{70}Ag_{30}$	
		$Au_{80}Ag_{20}$	
	Ag @ Cu ($Ag_{30}Cu_{70}$ to $Ag_{70}Cu_{30}$, 3 combinations)	$Ag_{30}Cu_{70}$	13–15
		$Ag_{50}Cu_{50}$	
		$Ag_{70}Cu_{30}$	

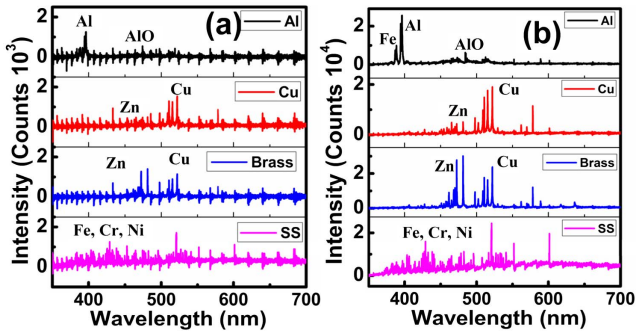

Fig. 2. Stack plots of the ST-FIBS spectra of metals; the alloys are recorded with an ICCD gain of (a) 1000 and (b) 2500.

prior to PCA analysis. Figures 3(a) and 3(b) illustrate the PC score plots of normalized (to maximum intensity) fs ST-FIBS spectra of metals at two ICCD gains of 1000, 2500 in the spectral range of 350–700 nm, and Figs. 3(c) and 3(d) depict the respective PCs. The first three PCs together accounted for 73% (60%, 10%, 3%) and 98% (74%, 21%, 3%) of the total variance associated, with the first PC being highest. Better grouping or clustering was achieved for the data with higher gain. This could be attributed to increase the SNR, which is also evident from the first three PCs, as shown in Figs. 3(c) and 3(d). In both the cases, PC1 and PC2 include the spectral features from Al, Cu, brass, and SS. However, PC3 (with gain 1000) resembles only a few spectral features (from Zn) buried in noise, compared to the one with high gain where Zn and Cu lines are clearly visible. Thus, the use of ICCDs facilitated the ST diagnosis by offering higher gain and broadband single shot analysis.

Figure 4(a) shows the normalized fs ST-FIBS spectra of an $Ag_{30}Cu_{70}$ bimetallic strip in a spectral region of 480–840 nm (with break in 590–755 nm) with ionic and atomic peaks of Ag and Cu labeled with the aid of the NIST database [31]. Figure 4(b) illustrates the variation of Ag and Cu atomic peaks (Ag I 520.91 nm, Cu I 521.82 nm) with varying concentrations of Ag and Cu. Normalized peak intensities exactly reflected the bimetallic weight percentage with Ag I peak intensity being highest in $Ag_{70}Cu_{30}$, equal in $Ag_{50}Cu_{50}$ and lowest in $Ag_{30}Cu_{70}$, when compared to Cu I 521.82 nm peak. Figures 4(c) and 4(d) illustrate the PC score plot and the first three PCs of normalized fs ST-FIBS spectra of Ag@Cu bimetallic targets in a 470–650 nm spectral range. The first three PCs accounted for 71% of the total variance (54%, 13%, 4%) present in the dataset. However, the classification can be improved by avoiding the spectral range which does not include any spectral features. The essential spectral features contributing for classification or discrimination are from both copper and silver.

A set of seven Ag@Au bimetallic targets (with varying weight percentages) were investigated in the same ST-FIBS configuration. Figure 5(a) depicts typical normalized ST-FIBS spectra of an $Ag_{20}Au_{80}$ bimetallic strip in a spectral region from of 400 to 700 nm. Ag and Au transitions were identified and labeled using the NIST database [31]. Most of the persistent atomic and ionic transitions of Au lie in the UV spectral region and, therefore, the observed Au transitions in visible region are weak. However, one persistent atomic transition of Au was observed at 627.81 nm, along with Au I 406.5 nm and Au I 479.25 nm, which are relatively strong transitions. Figure 5(b) data demonstrate that the Au I (627.81 nm) peak intensity increased linearly with an increase in the weight percentage of Au (i.e., from $Ag_{80}Au_{20}$ to $Ag_{20}Au_{80}$). Figures 5(c) and 5(d) illustrate the PC score plot and the first three PCs of normalized fs ST-FIBS spectra of Ag@Au bimetallic targets, respectively, in the 400–650 nm spectral range obtained from PCA analysis. The first three PCs accounted for 63% of total variance

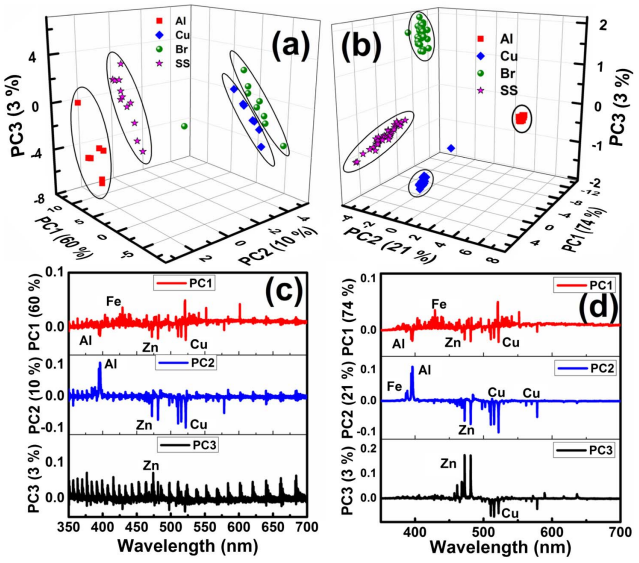

Fig. 3. PC score plots of ST-FIBS spectra of metals with an ICCD gain of (a) 1000 and (b) 2500; (c), (d) represent the PCs.

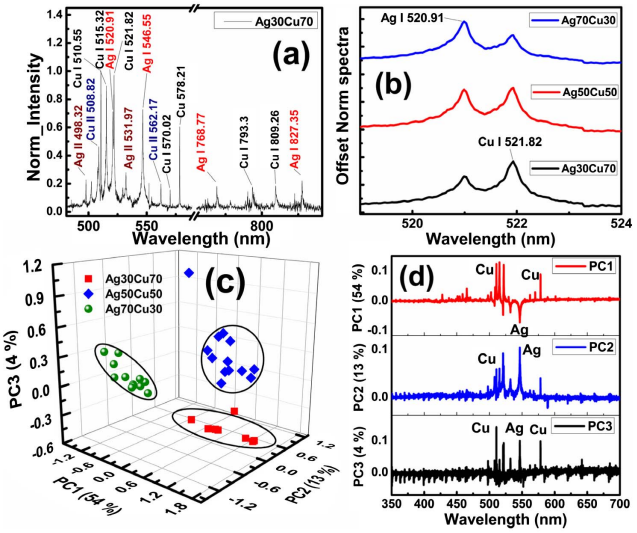

Fig. 4. (a) ST-FIBS spectra of $Ag_{30}Cu_{70}$ bimetallic strips, (b) intensity variation of Ag I (520.91 nm) and Cu I (521.82 nm) peaks in bimetallic strips, (c) PC score plot, and (d) PCs of ST-FIBS spectra of Ag@Cu bimetallic targets obtained from PCA analysis.

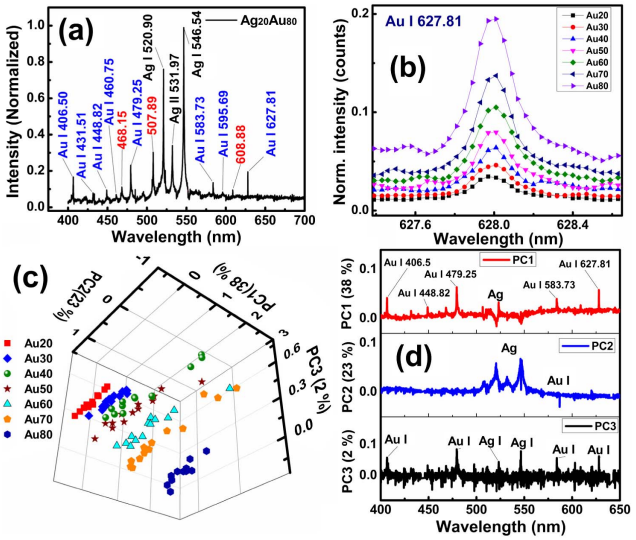

Fig. 5. (a) Representative fs ST-FIBS spectra of a $Ag_{20}Au_{80}$ bimetallic strip. (b) Intensity variation of Ag I (627.81 nm) peak with variation of Ag weight percentage. (c) PC score plot and (d) PCs obtained from PCA of Ag@Au bimetallic targets.

(38%, 23%, 2%) present in the dataset. The first PC depicts the essential spectral features from both silver and gold contributing towards the classification or discrimination.

The second PC was dominated by the spectral features of Ag. Even though the Au I emission intensities in ST-FIBS were relatively weaker (because of the absence of persistent transitions in the visible region), the achieved classification of Ag@Au bimetallic strips using PCA is promising. Finally, the classification or clustering efficiency of PCA was evaluated for all processed fs ST-FIBS spectra of metals and bimetallic strips in the spectral range of 350–700 nm. Figure 6(a) represents the PC score plot of metals and bimetallic targets. The first three PCs accounted for 92% (56%, 21%, 15%) of the total variance present in the dataset. Figure 6(b) presents the first three PCs that contain the essential spectral features which contribute for the classification. Out of these PCs, the first PC is like SS with transitions of Fe and has Cu, Zn, Al, and Ag spectral components. The second PC has spectral features from Al, Zn, and Ag whereas third PC has spectral components from Al, Zn, Ag, and Cu. Although Ag@Cu are well separated (encircled together in an ellipse), Ag@Au are not well resolved (shown in square). This could be attributed to the smaller contribution of weak transitions of Au I, which are present in fs ST-FIBS spectra of Ag@Au bimetallic strips, towards the total variance when all targets were analyzed together. However, employing flat field correction (eliminating diffraction orders on an ICCD image) [32], supervised or generic algorithms could possibly result in superior classification. Furthermore, employing telescopes with good transmission in the UV-visible range will support qualitative and quantitative measurements in the ST mode.

In summary, we have successfully demonstrated 6.5 m ST analysis of metals and bimetallic alloy targets using the ST-FIBS technique in laboratory conditions. A Schmidt–Cassegrain telescope with good transmission in the visible range was used to collect the plasma emission. The results obtained from PCA analysis clearly demonstrated that the ST-FIBS technique is adept in classifying targets with similar composition though, in some cases, there was a small overlap in the grouping. However, supervised algorithms such as partial least squares discriminant analysis or soft independent modeling by class analogy can further be implemented for enhanced class wise labeling. The variation in characteristic intensities of constituent transitions in bimetallic targets with respect to their weight percentages demonstrated the promise of femtosecond filaments for ST analytical applications. Detailed studies on the types and properties of filaments produced and, consequently, their effects on the LIBS plasma will enable the development of an efficient technique for ST trace analysis of any material. Further studies are also warranted on optimizing the LIBS signal collection efficiency.

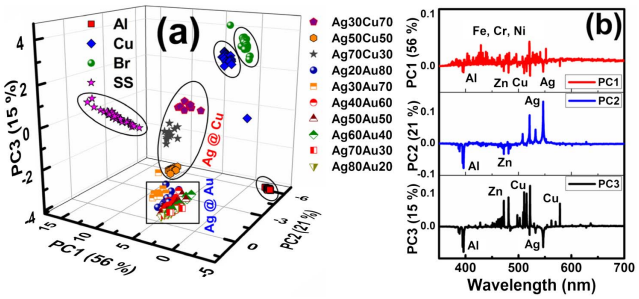

Fig. 6. (a) PC score plot of fs ST-FIBS spectra of metals and bimetallic targets; (b) represents the PCs.

Funding. Defence Research and Development Organisation (DRDO) (ERIP/ER/1501138/M/01/319/D (RD)); Board of Research in Nuclear Sciences (BRNS) (34/14/48/2014-BRNS/2084).

Acknowledgment. S. V. Rao acknowledges the financial support of DRDO, India.

REFERENCES

1. D. A. Cremers, F. Y. Yueh, J. P. Singh, and H. Zhang, *Laser-Induced Breakdown Spectroscopy, Elemental Analysis* (Wiley, 2006).
2. S. Harilal, B. Brumfield, N. LaHaye, K. Hartig, and M. Phillips, Appl. Phys. Rev. **5**, 021301 (2018).
3. K. E. Brown, M. T. Greenfield, S. D. McGrane, and D. S. Moore, Anal. Bioanal. Chem. **408**, 35 (2016).
4. K. E. Brown, M. T. Greenfield, S. D. McGrane, and D. S. Moore, Anal. Bioanal. Chem. **408**, 49 (2016).
5. S. Harilal, B. Brumfield, and M. Phillips, Opt. Lett. **43**, 1055 (2018).
6. L. A. Álvarez-Trujillo, V. Lazic, J. Moros, and J. J. Laserna, Appl. Opt. **56**, 3773 (2017).
7. R. C. Wiens, S. Maurice, B. Barraclough, M. Saccoccio, and W. C. Barkley, Space Sci. Rev. **170**, 167 (2012).
8. K. Stelmaszczyk, P. Rohwetter, G. Méjean, J. Yu, E. Salmon, J. Kasparian, R. Ackermann, J. P. Wolf, and L. Wöste, Appl. Phys. Lett. **85**, 3977 (2004).
9. A. Couairon and A. Mysyrowicz, Phys. Rep. **441**, 47 (2007).
10. S. Chin, S. Hosseini, W. Liu, Q. Luo, F. Théberge, N. Aközbek, A. Becker, V. Kandidov, O. Kosareva, and H. Schröder, Can. J. Phys. **83**, 863 (2005).
11. T. Fujii, N. Goto, M. Miki, T. Nayuki, and K. Nemoto, Opt. Lett. **31**, 3456 (2006).
12. J. L. Gottfried, J. F. C. De Lucia, C. A. Munson, and A. W. Miziolek, Appl. Spectrosc. **62**, 353 (2008).
13. K. C. Hartig, I. Ghebregziabher, and I. Jovanovic, Sci. Rep. **7**, 43852 (2017).
14. J. J. Laserna, R. F. Reyes, R. González, L. Tobaria, and P. Lucena, Opt. Express **17**, 10265 (2009).
15. M. Fisher, C. Siders, E. Johnson, O. Andrusyak, C. Brown, and M. Richardson, Proc. SPIE **6219**, 621907 (2006).
16. S. A. Kalam, N. L. Murthy, P. Mathi, N. Kommu, A. K. Singh, and S. V. Rao, J. Anal. At. Spectrom. **32**, 1535 (2017).
17. T. A. Labutin, V. N. Lednev, A. A. Ilyin, and A. M. Popov, J. Anal. At. Spectrom. **31**, 90 (2016).
18. A. K. Shaik, N. R. Epuru, H. Syed, C. Byram, and V. R. Soma, Opt. Express **26**, 8069 (2018).
19. I. Ghebregziabher, K. C. Hartig, and I. Jovanovic, Opt. Express **24**, 5263 (2016).
20. M. Weidman, M. Ramme, B. Bousquet, K. Lim, M. Durand, M. Baudelet, and M. Richardson, Opt. Lett. **40**, 4548 (2015).
21. https://www.celestron.com/pages/starbright-xlt-optical-coatings#.
22. C. Byram and V. R. Soma, Nano-Struct. Nano-Objects **12**, 121 (2017).
23. S. S. Harilal, B. E. Brumfield, B. D. Cannon, and M. C. Phillips, Anal. Chem. **88**, 2296 (2016).
24. S. S. Harilal, J. Yeak, B. E. Brumfield, and M. C. Phillips, Opt. Express **24**, 17941 (2016).
25. M. Rodriguez, R. Bourayou, G. Méjean, J. Kasparian, J. Yu, E. Salmon, A. Scholz, B. Stecklum, J. Eislöffel, U. Laux, A. P. Hatzes, R. Sauerbrey, L. Wöste, and J.-P. Wolf, Phys. Rev. E **69**, 036607 (2004).
26. J. Zabalza, J. Ren, J. Ren, Z. Liu, and S. Marshall, Appl. Opt. **53**, 4440 (2014).
27. A. K. Myakalwar, S. Sreedhar, I. Barman, N. C. Dingari, S. Venugopal Rao, P. Prem Kiran, S. P. Tewari, and G. M. Kumar, Talanta **87**, 53 (2011).
28. Y. Kim, Opt. Lett. **32**, 32 (2007).
29. D. Prochazka, M. Mazura, O. Samek, K. Rebrošová, P. Pořízka, J. Klus, P. Prochazková, J. Novotný, and J. Kaiser, Spectrochim. Acta B **139**, 6 (2018).
30. C. A. Munson, F. C. De Lucia, Jr., T. Piehler, K. L. McNesby, and A. W. Miziolek, Spectrochim. Acta B **60**, 1217 (2005).
31. https://www.nist.gov/pml/atomic-spectra-database.
32. T. C. Williams and C. R. Shaddix, Rev. Sci. Instrum. **78**, 123702 (2007).